Research Article

ADVANCED PHOTONICS

Chip-scale metalens microscope for wide-field and depth-of-field imaging

Xin Ye,[a,b] Xiao Qian,[a,b] Yuxin Chen,[a,b] Rui Yuan,[a] Xingjian Xiao,[a,b] Chen Chen,[a,b] Wei Hu,[a] Chunyu Huang,[a] Shining Zhu,[a,b] and Tao Li[a,b,*]

[a]Nanjing University, College of Engineering and Applied Sciences, National Laboratory of Solid State Microstructures, Key Laboratory of Intelligent Optical Sensing and Integration, Jiangsu Key Laboratory of Artificial Functional Materials, Nanjing, China
[b]Collaborative Innovation Center of Advanced Microstructures, Nanjing, China

Abstract. Microscopy is very important in research and industry, yet traditional optical microscopy suffers from the limited field-of-view (FOV) and depth-of-field (DOF) in high-resolution imaging. We demonstrate a simultaneous large FOV and DOF microscope imaging technology based on a chip-scale metalens device that is implemented by a SiN_x metalens array with a co- and cross-polarization multiplexed dual-phase design and dispersive spectrum zoom effect. A 4-mm × 4-mm FOV is obtained with a resolution of 1.74 μm and DOF of 200 μm within a wavelength range of 450 to 510 nm, which definitely exceeds the performance of traditional microscopes with the same resolution. Moreover, it is realized in a miniaturized compact prototype, showing an overall advantage for portable and convenient microscope technology.

Keywords: metalens; microscope; wide-field imaging.

Received May 21, 2022; revised manuscript received Jun. 12, 2022; accepted for publication Jul. 1, 2022; published online Jul. 27, 2022.

[DOI: 10.1117/1.AP.4.4.046006]

1 Introduction

Microscopes are important imaging tools that effectively expand the human eyes to the microworld for applications in scientific research, biomedical diagnosis, and industry. Besides the ultimate goal of superresolution, a new direction of this technique aims for wide field-of-view (FOV), large depth-of-field (DOF), high throughput, and compactly portable performance.[1–6] Traditional optical microscopes are established based on refractive optical elements[7,8] that are usually bulky and heavy with limitations in FOV and DOF, although they have been substantially developed. A possible solution to miniaturizing the imaging system is to use flat diffractive lenses, but the quite low efficiency and poor imaging quality prevent its imaging applications.[9] Recent lensless imaging technology considerably revolutionizes the manner of imaging technology and enables the possibility of highly compact imaging devices.[3,10–12] Nevertheless, it strongly depends on the postprocess computation that requires large resources and prior information with risk of artifacts in some cases.

A metalens, as a kind of metasurface composed of subwavelength units, opens a new avenue to access ultracompact and lightweight optical imaging systems.[13,14] According to the powerful capability in manipulating the phase, polarization, and amplitude of light,[15–22] versatile functional metasurfaces have been well demonstrated,[23–28] including image devices.[29–42] Among them, a recent approach of metalens-integrated imaging with a wide FOV shows a promising route to ultracompact and lightweight microscopes.[36] It was implemented by a polarization multiplexed metalens array directly mounted on a complementary metal-oxide semiconductor (CMOS) image sensor, which not only shows its highly compact advantage but also breaks the FOV constraint. Unfortunately, its imaging quality is relatively poor due to its low efficiency with background noises. Moreover, its overall FOV with respect to the corresponding resolution is still smaller than that of a traditional microscope, though it is very compact in device architecture.

In this work, we developed a polarizer-embedded metalens imaging device (PMID) that is implemented based on geometric silicon nitride (SiN_x) metasurfaces directly mounted on a CMOS image sensor. It is proved to significantly improve the imaging quality by eliminating the background noise, which

*Address all correspondence to Tao Li, taoli@nju.edu.cn

enables zoomed-in imaging to reach a higher resolution. After a systematic characterization of the imaging performances from the singlet metalens, we extended it to a metalens array with two sets of polarization multiplexed focusing phases that work in co- and cross-polarizations, respectively. Based on this design, the embedded circular polarization filter (CPF) can work for both orthogonal polarization illuminations to construct two sets of compensated subimages, which enables a stitched high-quality large FOV microscope image. Thanks to the broadband property, this metalens array inherits the dispersive spectral zoom effect[32,43] and shows the capability of large DOF imaging by tuning the illumination wavelength. A chip-scale (4 mm × 4 mm) FOV is obtained with the resolution of 1.74 μm (~1.37 μm in theory, limited by the size of the image sensor pixel), DOF of ~200 μm within a wavelength of 450 to 510 nm, which definitely exceeds the performance of traditional microscopes with the same resolution. Furthermore, it is fully implemented in a compact prototype with a light-emitting diode (LED) light source and a liquid-crystal polarization switch, which provides a non-mechanical, stable, and miniaturized microscope technique for portable and convenient applications.

2 Device Architecture and Metalens Design

Figure 1(a) shows the layered architecture of the chip-scale PMID. The chip-scale metalens and fixed CPF with a thickness of 220 μm are fixed on the CMOS image sensor (Imaging source: DMM 27UJ003-ML, pixel size: 1.67 μm × 1.67 μm) by two layers of optically clear adhesive tapes (OCA, thickness: 50 μm and 100 μm, Tesa, 69402). Here, the OCA works both as the connector and the spacer that determine the imaging distance (v), which is fixed in our chip-scale PMID. A photographic image is depicted in Fig. 1(b).

The phase profile of the metalens is designed according to the following hyperbolic distribution:[13]

$$\varphi = \frac{2\pi}{\lambda}\left(f - \sqrt{x^2 + y^2 + f^2}\right), \tag{1}$$

where λ is the design wavelength, x and y are the coordinates of each nanofin, and f is the focal length. This phase profile is imparted via the Pancharatnam–Berry (PB) phase.[16] Each nanofin of the metasurface is designed with a high-aspect-ratio rectangle with the same height ($h = 1$ μm), length ($l_x = 240$ nm), width ($l_y = 95$ nm), and arranged in period of $p = 300$ nm to satisfy the Nyquist–Shannon sampling theorem,[44] which operates as a half-wave-plate with a high transmission efficiency. SiN_x (refractive index of 2.0 at 470 nm) was chosen because of its low loss in visible light and its potential compatibility with full CMOS-based devices. The polarization conversion ratio (PCR) of nanofins, which is the ratio of the transmitted optical power with opposite helicity to the total incident power, is calculated to be 99% at 470 nm by a commercial finite-difference time-domain (FDTD) solver (Lumerical Inc., Vancouver, Canada). Three distinct 250-μm-diameter metalenses were fabricated with focal lengths equal to 360, 330, and 250 μm, corresponding to magnifications of 1×, 2×, and 3×, respectively. All metalenses were fabricated using standard electron-beam lithography and dry etching in a 1-μm-thick SiN_x film deposited on a fused silica substrate (refractive index of 1.48 at 470 nm, see Secs. S1 and S2 of the Supplementary Material). The inset of Fig. 1(b) shows the sideview scanning electron microscope (SEM) images of a fabricated SiN_x metalens.

3 Imaging Characterization of Singlet-Metalens PMID

Before getting to the large FOV imaging device, first, we characterized the imaging performances of a singlet-metalens PMID, including the resolution, signal-to-noise ratio (SNR), modulation transfer function (MTF), and imaging bandwidth. The experimental details are provided in Sec. S1 and Fig. S2 of the Supplementary Material. Note that we also measured a set of imaging performances with the same metalens imaging device but without the embedded CPF for comparison. Figures 1(c) and 1(d) show the images of a 1951 United States Air Force (USAF) resolution test chart taken through metalenses without/with CPF at different magnifications, respectively. Because CPF can filter out the background co-polarized light, the image quality (including SNR and resolution) with CPF is much better than that without CPF, especially under large magnification, as shown in Fig. 1(e). To quantitatively evaluate the quality of imaging, we defined $\mathrm{SNR} = 10\ \mathrm{lg}(I_{\mathrm{signal}}/I_{\mathrm{noise}})$, where I_{signal} and I_{noise} refer to the intensity of the signal that can be clearly resolved and the standard deviation of the background noise intensity, respectively. Next, we calculated SNR based on multiple sets of signals and noises for obtaining accurate SNR of two different conditions and reached average values of SNR = 23.46/30.37, 16.22/24.60, and 13.01/27.60 dB, respectively. The corresponding resolutions for three cases are 1.74 μm (limited by CMOS pixel size: 1.67 μm), 1.1 μm, and 870 nm at imaging distance $v = 720$, 1000, and 1000 μm, respectively, as shown in Fig. 1(g).

The MTFs of all metalenses are obtained by the slanted-edge method,[45] as shown in Fig. 1(f), which show a good agreement with theoretical MTF at a low spatial frequency in all metalenses. The discrepancies at a high spatial frequency probably contribute to the background noises. The slanted-edge method is to calculate the Fourier transform of the line spread function, which is the first derivative of the edge spread function (ESF) (i.e., $\mathrm{MTF} = |\mathcal{F}[\mathrm{dESF}/\mathrm{d}x]|$). Although the PMID has a fixed imaging distance, optical zoom can be realized to obtain depth information by tuning the working wavelength due to the chromatic dispersion of the metalens. The details are provided in Sec. S3 of the Supplementary Material.

4 Dual-Phase Design for Co- and Cross-Polarization

In our previous work, a polarization multiplexed dual-phase metalens array was proposed and implemented in the CMOS integrated imaging device.[36] It successfully expanded the FOV without increasing the working distance, and the intersecting dual-phase effectively compensated the blind areas in imaging stitching. However, the dual-phase design was based on two orthogonal polarizations that cannot work under a fixed CPF embedded in the integrated device. It led to a relatively poor imaging quality in imaging contrast and SNR, since the PB phase efficiency cannot reach the unity and results in inevitable background noises.

Figure 1(d) has shown the significant improvements in PMID imaging quality by adding the CPF compared with that without CPF [see Fig. 1(c)], and it is necessary to validate it in the polarization multiplexed lens array. To circumvent this problem, we proposed a new kind of polarization multiplexed metalens design that can modulate the co- and cross-polarized light independently by combining the propagation and PB phase. In a circle base, the Jones matrix of nanofin in a metasurface

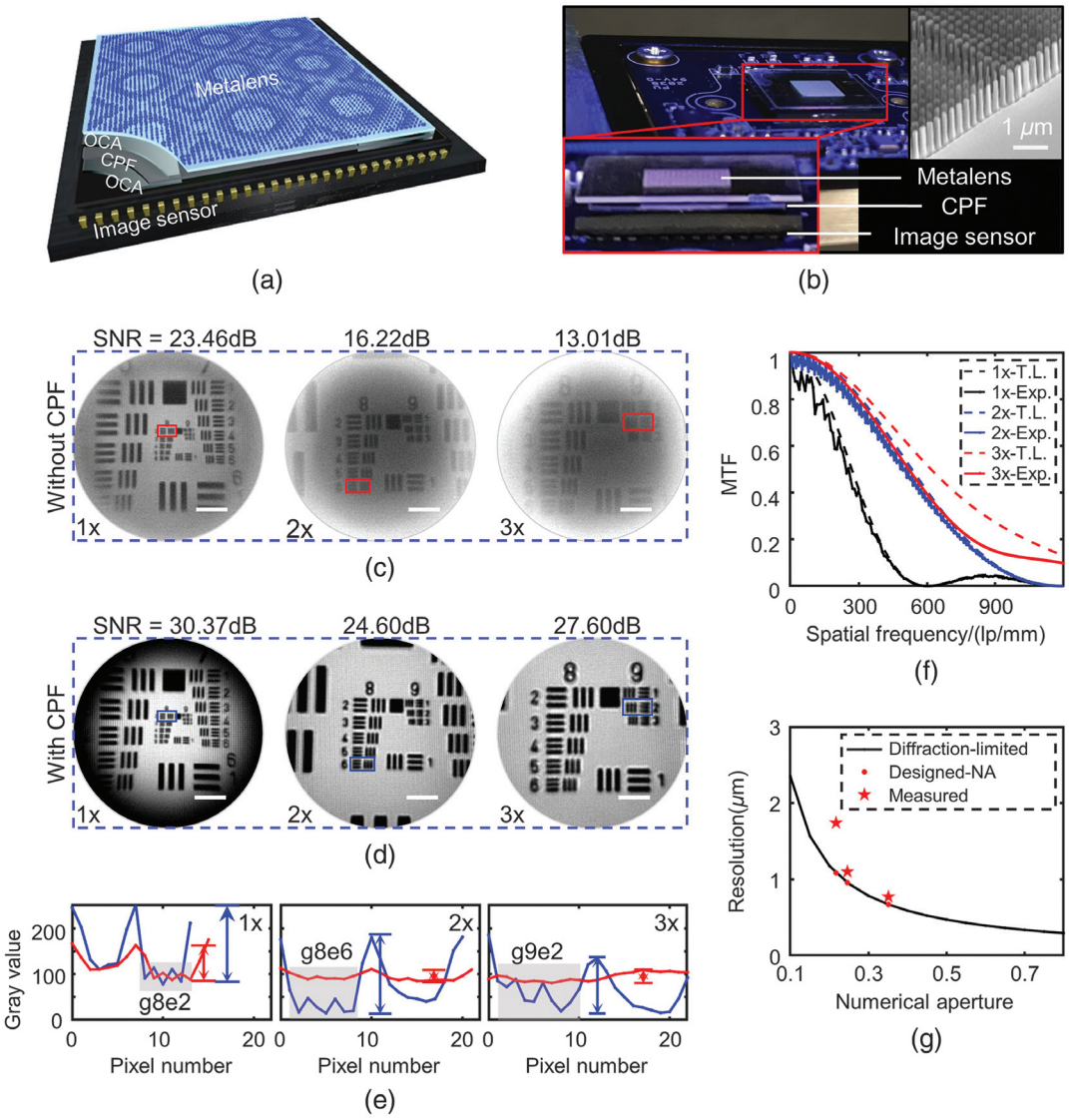

Fig. 1 Architecture and characterization of PMID. (a) Schematic of the chip-scale PMID. (b) Photographic image of the PMID with bottom-left inset for the side-view of the zoomed-in image, and upper-right inset for the SEM image of the SiN_x metalens. (c) Imaging results of USAF resolution chart taken through the metalenses without CPF in 1×, 2×, 3× image magnifications, whose NA = 0.33, 0.35, and 0.45, with SNR equal to 23.46, 16.22, and 13.01 dB, respectively. (d) The counterpart images taken through the PMID (with the CPF) with respect to (c) resulting in SNR = 30.37, 24.60, 27.60 dB, respectively. Scale bar: 50 μm. (e) The intensity distributions of horizontal lines (HLs) of in red/blue solid boxes in (c) and (d), corresponding to the resolution elements of g8e2 (1.74 μm), g8e6 (1.1 μm), and HL of g9e2 (870 nm), respectively, for three cases. (f) The experimental and theoretically limited MTF of three imaging results. (g) Measured resolution of singlet-metalens PMIDs with different NA. The black line is the diffraction-limited, while the red stars are the experimental results and the red points in the black line are the theoretical resolutions of the designed metalenses.

describing the relation between the input electric field (E_{in}) and the output electric field (E_{out}) can be written as[27]

$$J = R(-\theta)\begin{bmatrix} e^{i\phi_{RR}} & e^{i\phi_{LR}} \\ e^{i\phi_{RL}} & e^{i\phi_{LL}} \end{bmatrix} R(\theta) = \begin{bmatrix} e^{i\phi_{RR}} & e^{i(2\theta+\phi_{LR})} \\ e^{i(-2\theta+\phi_{RL})} & e^{i\phi_{LL}} \end{bmatrix}, \quad (2)$$

where ϕ_{RR}, ϕ_{RL}, ϕ_{LR}, and ϕ_{LL} are the propagation phases, and $R(\theta)$ is a 2×2 rotation matrix. In this work, the widely used rectangular nanofins are chosen, where the phase shift $\phi_{RR} = \phi_{LL}$ and $\phi_{RL} = \phi_{LR}$ due to the mirror symmetry. So, when the incident light is right-handed circularly polarized (RCP), E_{out} becomes

$$E_{out} = JE_{in} = \begin{bmatrix} e^{i\phi_{RR}} & e^{i(2\theta+\phi_{LR})} \\ e^{i(-2\theta+\phi_{RL})} & e^{i\phi_{LL}} \end{bmatrix} \begin{bmatrix} 1 \\ 0 \end{bmatrix} = \begin{bmatrix} e^{i\phi_{RR}} \\ e^{i(-2\theta+\phi_{RL})} \end{bmatrix}. \quad (3)$$

Similarly, for the left-handed circularly polarized (LCP):

$$E_{\text{out}} = JE_{\text{in}} = \begin{bmatrix} e^{i\phi_{\text{RR}}} & e^{i(2\theta+\phi_{\text{LR}})} \\ e^{i(-2\theta+\phi_{\text{RL}})} & e^{i\phi_{\text{LL}}} \end{bmatrix} \begin{bmatrix} 0 \\ 1 \end{bmatrix} = \begin{bmatrix} e^{i(2\theta+\phi_{\text{LR}})} \\ e^{i\phi_{\text{LL}}} \end{bmatrix}. \tag{4}$$

From Eqs. (3) and (4), we can derive the phase modulations for the output RCP/LCP light respectively under diverse incident RCP or LCP light, which means that co- and cross-polarized light can be independently modulated due to the independent ϕ_{RR} and ϕ_{RL} (ϕ_{LR} and ϕ_{LL}).

By adopting this design to our integrated scheme, two independent phase profiles can be obtained on output with a fixed polarization filter. For example, if the output light is set as RCP, then the incident RCP light can be designed for a special function with the phase profile $\varphi_1(x, y) = \phi_{\text{RR}}(x, y)$ and the incident

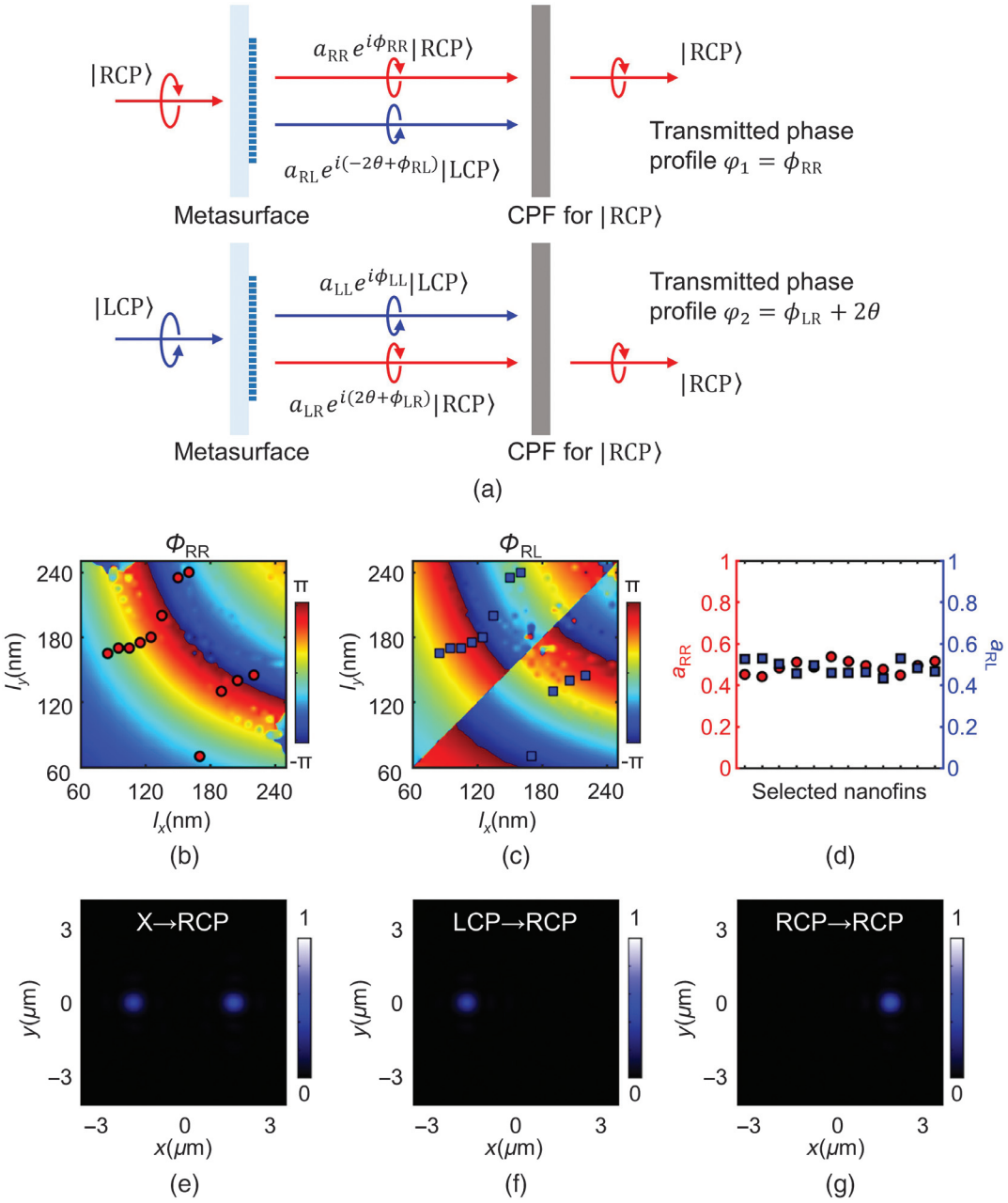

Fig. 2 Independent dual-phase design for co- and cross-circularly polarized light. (a) Schematics of the design principle: a single metasurface obtains two independent phase modulations for each incident circular polarization light after fixed CPF (for RCP). Simulated phase responses of the transmitted (b) RCP and (c) LCP light with the nanofins structural parameters under RCP incidence. (d) Amplitude distribution of the selected nanofin structures, where red circles and blue squares correspond to co-polarized (b) and cross-polarized (c) phase modulations, respectively. The simulated intensity distributions of a transverse bifocal metalens on the focal plane with CPF for (e) *x*-polarized, (f) LCP, and (g) RCP light incidence.

LCP light with another phase profile $\varphi_2(x,y) = \phi_{LR}(x,y) + 2\theta(x,y)$. In that case, we can achieve a new polarization-switchable metasurface. The schematics of the electric field change of our design are shown in Fig. 2(a); the output light can be written as $a_{RR}e^{i\phi_{RR}}|RCP\rangle$ and $a_{LR}e^{i(2\theta+\phi_{LR})}|RCP\rangle$ under two orthogonal circularly polarized light beams, where a_{RR} and a_{LR} are the corresponding amplitudes of the output beams. For analyzing the amplitudes of the output light, focus on a single nanofin. When illuminated by a circularly polarized light, the transmitted light can be expressed as[46]

$$T(\theta) = \frac{t_x + t_y}{2}\begin{bmatrix} 1 \\ \pm i \end{bmatrix} + \frac{t_x - t_y}{2} e^{\pm i2\theta}\begin{bmatrix} 1 \\ \mp i \end{bmatrix}, \tag{5}$$

where t_x and t_y are the complex amplitudes of the incident light polarized along each axis written as $t_x = \sqrt{T_x}e^{i\phi x}$, $t_y = \sqrt{T_y}e^{i\phi y}$. Equation (5) shows that the helicity of a part of the transmitted light is the same as incidence and the other is the opposite. Then, we can get $a_{RR} = |(t_x + t_y)/2|$ and $a_{LR} = |(t_x - t_y)/2|$ based on which we can obtain the transmitted efficiencies of co-polarization and cross-polarization as ${a_{RR}}^2$ and ${a_{LR}}^2$, respectively.

In the PMID, it is best to have ${a_{RR}}^2 \approx {a_{LR}}^2$ to ensure the PCR ≈ 0.5 to get comparable intensities in two polarization states. The simulated phase responses of nanofins for the transmitted RCP and LCP light are shown in Figs. 2(b) and 2(c), respectively. The red circles and blue squares correspond to co-polarized and cross-polarized manipulations of the selected nanofins with the required phase responses. Figure 2(d) shows the amplitude distribution of the selected nanofins. By selecting a suitable size and orientation angle of nanofins, the phase manipulation is completely decoupled for two incident circularly polarized light beams. As a proof of concept, we simulated the response of a transverse bifocal metalens with a focal length of 9 μm, radius r of 3.75 μm, and focal shift distance of $\pm r/2$ by FDTD. The simulation intensity profiles on the focal plane with CPF for x-polarized, LCP, and RCP light incidence are shown in Figs. 2(e)–2(g), respectively, and are exactly consistent with the design.

5 Wide-Field and Depth-of-Field Imaging by Chip-Scale PMID

Based on the co- and cross-polarization multiplexed metalens array, we proposed and implemented a chip-scale PMID in a 4f

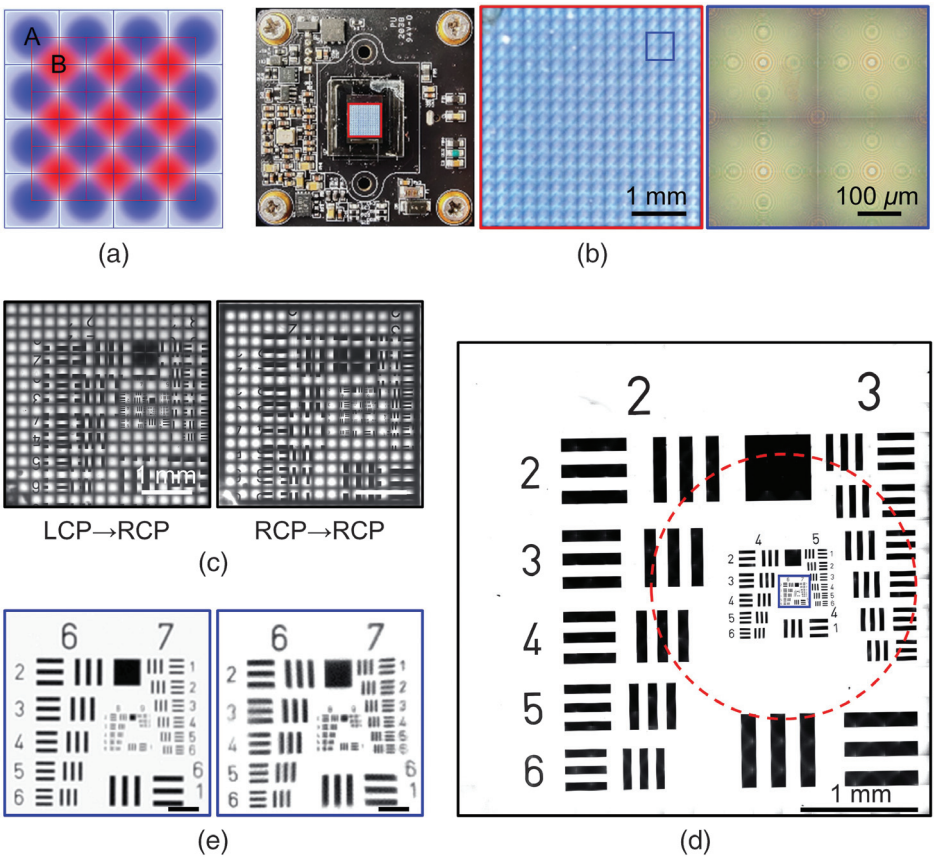

Fig. 3 Imaging of the chip-scale PMID. (a) Phase distribution of part of the chip-scale metalens in the x–y plane. The lattice A (blue) and lattice B (red) correspond to the phase distributions for LCP and RCP light incidence, respectively. (b) Top-view photographic images of the chip-scale PMID (left), the 16 × 16 metalens array (middle), and optical microscope image of a 2 × 2 metalens array (right). (c) Raw images of the USAF resolution test chart with LCP and RCP light incidence. (d) Stitched image from subimages of (c). The region in the red circle corresponds to the FOV of the microscope. (e) Zoomed-in stitched image (right) and image obtained with the Olympus microscope (10×, NA = 0.25) (left) to show the resolution. Scale bar: 40 μm.

system with an FOV of 4 mm × 4 mm. The phase profiles of the metalens satisfy the requirements of two different focusing lenses for two orthogonal circularly polarized light beams, as schematically shown in Fig. 3(a) (more details about the design of a chip-scale metalens are provided in Sec. S4 of the Supplementary Material), where the lattices A and B correspond to the focusing phase distributions under LCP and RCP incidences, respectively. Each metalens is designed at 470 nm with focal lengths equal to 360 μm and diameters of 250 μm. Then, these metalenses compose a 16 × 16 focusing array for LCP and 15 × 15 ones for RCP incidence according to the dual-phase design. The entire metalens region is about 4 mm × 4 mm, nearly covering the whole surface of a CMOS image sensor (6.440 mm × 4.616 mm), as shown in the left image of Fig. 3(b). The middle and right images of Fig. 3(b) show the top-view photographic image of the whole metalens array and the zoomed-in image of the metalens array, respectively. By simply switching the polarization station of incident light, we can obtain two independent images of the USAF resolution test chart taken by the imaging device, as displayed in Fig. 3(c). Figure 3(d) shows a stitched image by combining two sets of subimages after certain image processing (the detailed proceeding is provided in Sec. S5 of the Supplementary Material), of which the region in the red circle corresponds to the FOV of an Olympus microscope with a 10× objective (NA = 0.25). The stitched image has a wide FOV area the same as the metalens array region (4 mm × 4 mm) with the same resolution of a single metalens (~1.74 μm, g8e2). Here, we calculated the space-bandwidth product (SBP) to compare the performance of the chip-scale PMID and traditional Olympus microscope, which refers to the effective number of pixels required to represent an image and is a measure of the information content of the imaging system.[44] The SBP of the chip-scale PMID is ~21.1, which is >18.4 of the traditional microscope with a 10× objective. Figure 3(e) shows the zoomed-in image with the same imaging resolution taken through the PMID (right) and a commercial Olympus microscope (left), respectively. The performance of this PMID is comparable to that of the traditional microscope with the same resolution, and it evidently shows the great improvement (~4 times) in FOV of PMID without decreasing the imaging quality.

This chip-scale PMID is further employed to image different biospecimens. To observe the cells in the solution, we made a cell solution container with glass cover (0.13 to 0.16 mm) and ultraviolet (UV) adhesive, of which the diagram and photographic image are displayed in Figs. 4(a) and 4(b), respectively. Figure 4(c) shows the stitched image of human umbilical vein endothelial cells (HUVECs) in a solution at λ = 470 nm. This stitched image covers 256× times the area of a singlet metalens without decreasing the resolution. Next, we changed the working wavelength from 450 to 510 nm to derive DOF information owing to the spectral zooming effect. Zoomed-in images of the HUVECs at different operating wavelengths are shown in Fig. 4(d) from which different microscopic cell information at different depths in the solution can be distinguished. According to our characterization, the total DOF is measured at about 200 μm. (More details are provided in Sec. S6 of the Supplementary Material.) Note that compared with the previous version of the metalens microscope,[36] this PMID integrating the CPF gives rise to a high SNR and imaging quality and makes it possible to achieve broadband imaging to resolve the DOF information in a wide-field scheme. So far, based on this chip-scale PMID we have achieved good resolution, high SNR, large FOV, and tunable DOF imaging simultaneously. Moreover, this device also enables wide view living videos for microscopic observations; see Video 1 for flowing HUVECs in a solution as an example.

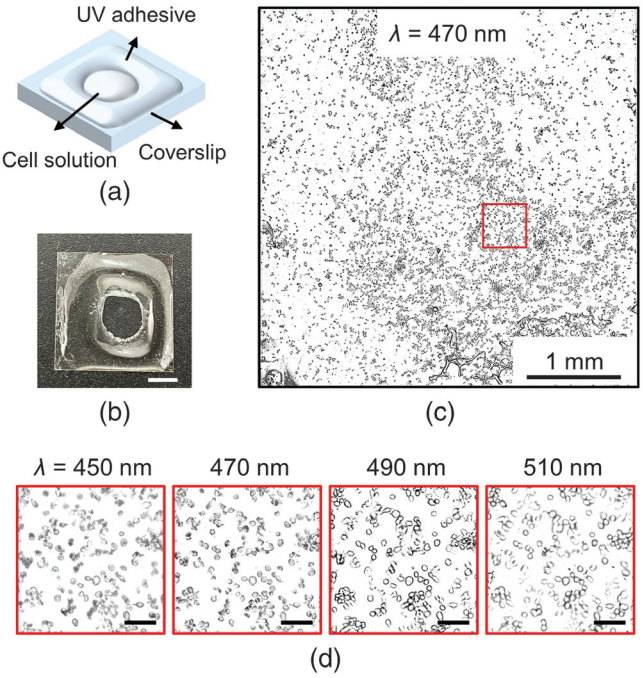

Fig. 4 Wide-field and DOF imaging. (a) Schematic of the cell solution container. (b) Top-view photographic image of the cell solution container. Scale bar: 5 mm. (c) Stitched image of HUVECs in solution. (d) Zoomed-in images of the red box in (c) at 450, 470, 490, and 510 nm, respectively. Scale bar: 100 μm. Wide view living observations of flowing HUVECs in a solution with PMID (Video 1, MP4, 7.17 MB [URL: https://doi.org/10.1117/1.AP.4.4.046006.1]).

To further demonstrate the advantage of the chip-scale PMID for integration, we implemented a miniaturized compact prototype with a combination of the LED light source, liquid crystal polarizer, and sample holder as its image shown in Fig. 5(b). It has a very compact size of 3 cm × 3.5 cm × 4 cm, with a 1000-fold reduction in size and weight as compared with the bulky Olympus microscope [see Fig. 5(a)], so it is termed as a portable microscope system (PMS). Note that in this PMS, a liquid crystal (LC) is adopted together with a polarizer and blue-light LED (λ ~ 470 nm) source to provide a non-mechanical switch of illumination polarization. Based on this PMS, a wide-field microscopic image can be achieved as well. For example, Fig. 5(c) shows the results of the pine stem cross section (c.s.), where all feature sizes can be clearly distinguished with a high imaging quality by comparing with the image (decolored) taken by the Olympus microscope (10×). Meanwhile, the full FOV of the PMS is ~7.5 times the FOV of the Olympus microscope camera with a 10× objective. Undoubtedly, this PMID-enabled PMS prototype has shown its overwhelming advantage in portable and convenient microscope imaging. There are more details about PMS in Sec. S7 of the Supplementary Material and Video 2.

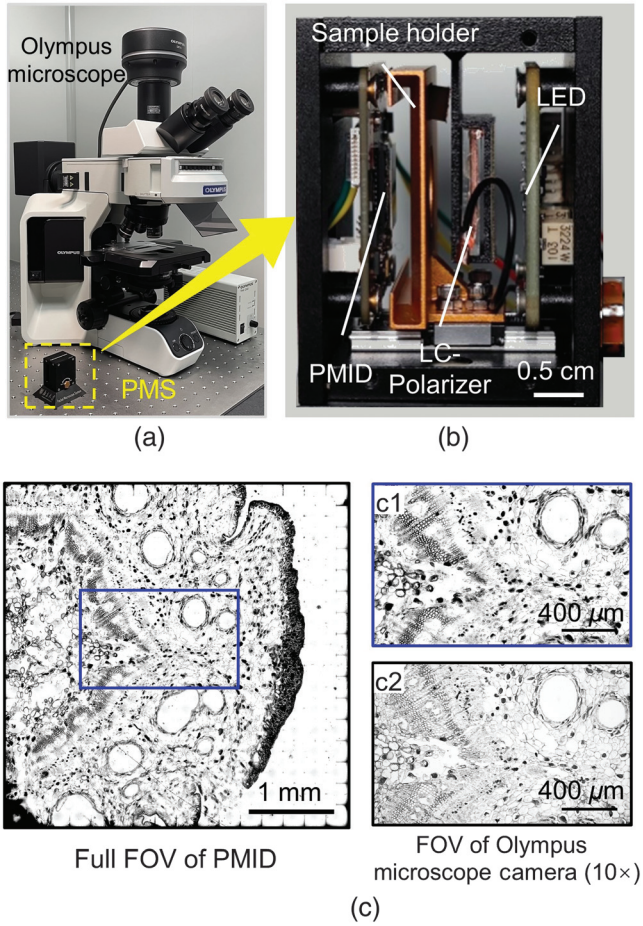

Fig. 5 Compact prototype of the chip-scale PMID. (a) Photographic image of the traditional Olympus microscope together with the PMS prototype. (b) Photographic image of the PMS prototype (3 cm × 3.5 cm × 4 cm). (c) Stitched image of pine stem c.s. at 470 nm. Zoomed-in image (c1) and image (c2) taken by the Olympus microscope (10×). The operation of PMS (Video 2, MP4, 11.7 MB [URL: https://doi.org/10.1117/1.AP.4.4.046006.2]).

6 Discussion and Conclusion

We have proposed a PMID for wide-field and DOF imaging via integrating both SiN_x metalenses and CPF directly to a CMOS image sensor. A new kind of polarization-multiplexed metalens was proposed to modulate the co- and cross-polarized light independently, which rightly enables the fixed polarization filter to work for the integrated device. Detailed characterizations of imaging performances of the singlet SiN_x metalenses, including the SNR, MTF, resolution, and imaging bandwidth were systematically performed and carefully compared with the counterpart without CPF. As a result, we successfully demonstrated a chip-scale PMID with the resolution of 1.74 μm, an FOV of 4 mm × 4 mm, and DOF of ~200 μm, verifying the advantage of wide-field and DOF imaging over the traditional microscope at the same resolution. To the best of our knowledge, this is the first metalens microscope that has an FOV larger than the mature traditional ones, and the DOF tuning without mechanical motion is also a striking feature in large FOV imaging. In the meantime, the miniaturized PMS prototype has a 1000-fold reduction in volume and weight of the traditional. It should be mentioned that the current resolution (1.74 μm) of PMID is not limited by the metalens but the pixel size (1.67 μm) of the CMOS image sensor in our 4f imaging system, which would possibly be improved by employing a smaller pixel-sized CMOS sensor with further development of CMOS technology. The other possibility of improving the resolution could be the booming computational imaging techniques, which have been proved to be an efficient method in many cases of upgrading the imaging performance. Frankly, our microscope imaging function based on two circularly-polarized light will be affected with respect to the circular-polarization sensitive objects, in which some subimages will be possibly weaken or even absent. For these cases, there is still an alternative solution by changing the metalens array design from the circular polarization multiplexing to the linear polarization multiplexing (i.e., x- and y-polarizations), then it is valid to work in the circular polarization-sensitive objects.[21] This chip-scale microscope has shown its overwhelming advantages not only in large FOV and DOF but also the compactness compared with the traditional optical microscope, which will undoubtedly illuminate new revolutionary optical devices by meta-technology.

Acknowledgments

The authors thank Dr. Zuoxiu Tie and Dr. Wei Jiang for the help in preparing cell samples. The authors acknowledge financial support from the National Key R&D Program of China (2017YFA0303701) and the National Natural Science Foundation of China (91850204 and 12174186). Tao Li acknowledges support from the Dengfeng Project B of Nanjing University. The authors declare no competing financial interest.

References

1. Ø. I. Helle et al., "Structured illumination microscopy using a photonic chip," *Nat. Photonics* **14**, 431–438 (2020).
2. A. Archetti et al., "Waveguide-PAINT offers an open platform for large field-of-view super-resolution imaging," *Nat. Commun.* **10**, 1267 (2019).
3. T.-W. Su, L. Xue, and A. Ozcan, "High-throughput lensfree 3D tracking of human sperms reveals rare statistics of helical trajectories," *Proc. Natl. Acad. Sci. U. S. A.* **109**, 16018–16022 (2012).
4. X. Liu et al., "Fluorescent nanowire ring illumination for wide-field far-field subdiffraction imaging," *Phys. Rev. Lett.* **118**, 076101 (2017).
5. G. Zheng, R. Horstmeyer, and C. Yang, "Wide-field, high-resolution Fourier ptychographic microscopy," *Nat. Photonics* **7**, 739–745 (2013).
6. K. C. Lee et al., "A smartphone-based Fourier ptychographic microscope using the display screen for illumination," *ACS Photonics* **8**, 1307–1315 (2021).
7. W. J. Smith, *Modern Lens Design*, McGraw-Hill, New York (2004).
8. H. Gross, F. Blechinger, and B. Achtner, *Handbook of Optical Systems*, Wiley-VCH, Weinheim (2005).
9. D. C. O'Shea et al., *Diffractive Optics: Design, Fabrication, and Test*, SPIE Press, Bellingham, Washington (2003).
10. G. Jin et al., "Lens-free shadow image based high-throughput continuous cell monitoring technique," *Biosens. Bioelectron.* **38**, 126–131 (2012).
11. A. C. Sobieranski et al., "Portable lensless wide-field microscopy imaging platform based on digital inline holography and multi-frame pixel super-resolution," *Light Sci. Appl.* **4**, e346 (2015).
12. A. Ozcan and E. McLeod, "Lensless imaging and sensing," *Annu. Rev. Biomed. Eng.* **18**, 77–102 (2016).

13. M. Khorasaninejad et al., "Metalenses at visible wavelengths: diffraction-limited focusing and subwavelength resolution imaging," *Science* **352**, 1190–1194 (2016).
14. W. T. Chen, A. Y. Zhu, and F. Capasso, "Flat optics with dispersion-engineered metasurfaces," *Nat. Rev. Mater.* **5**, 604–620 (2020).
15. N. Yu et al., "Light propagation with phase discontinuities: generalized laws of reflection and refraction," *Science* **334**, 333–337 (2011).
16. L. Huang et al., "Dispersionless phase discontinuities for controlling light propagation," *Nano Lett.* **12**, 5750–5755 (2012).
17. S. Sun et al., "High-efficiency broadband anomalous reflection by gradient meta-surfaces," *Nano Lett.* **12**, 6223–6229 (2012).
18. N. Yu and F. Capasso, "Flat optics with designer metasurfaces," *Nat. Mater.* **13**, 139–150 (2014).
19. A. Arbabi et al., "Dielectric metasurfaces for complete control of phase and polarization with subwavelength spatial resolution and high transmission," *Nat. Nanotechnol.* **10**, 937–943 (2015).
20. S. M. Kamali et al., "A review of dielectric optical metasurfaces for wavefront control," *Nanophotonics* **7**, 1041–1068 (2018).
21. H. Wang et al., "Independent phase manipulation of co- and cross-polarizations with all-dielectric metasurface," *Chin. Opt. Lett.* **19**, 053601 (2021).
22. J. Li et al., "Dual-band independent phase control based on high efficiency metasurface," *Chin. Opt. Lett.* **19**, 100501 (2021).
23. M. Khorasaninejad and F. Capasso, "Metalenses: versatile multifunctional photonic components," *Science* **358**, eaam8100 (2017).
24. M. Faraji-Dana et al., "Compact folded metasurface spectrometer," *Nat. Commun.* **9**, 4196 (2018).
25. E. Arbabi et al., "Full-Stokes imaging polarimetry using dielectric metasurfaces," *ACS Photonics* **5**, 3132–3140 (2018).
26. Y. Zhou et al., "Flat optics for image differentiation," *Nat. Photonics* **14**, 316–323 (2020).
27. C. Chen et al., "Highly efficient metasurface quarter-wave plate with wave front engineering," *Adv. Photonics Res.* **2**, 2000154 (2021).
28. M. Miyata et al., "Full-color-sorting metalenses for high-sensitivity image sensors," *Optica* **8**, 1596–1604 (2021).
29. A. Arbabi et al., "Miniature optical planar camera based on a wide-angle metasurface doublet corrected for monochromatic aberrations," *Nat. Commun.* **7**, 13682 (2016).
30. S. Wang et al., "Broadband achromatic optical metasurface devices," *Nat. Commun.* **8**, 187 (2017).
31. E. Arbabi et al., "MEMS-tunable dielectric metasurface lens," *Nat. Commun.* **9**, 812 (2018).
32. C. Chen et al., "Spectral tomographic imaging with aplanatic metalens," *Light Sci. Appl.* **8**, 99 (2019).
33. R. J. Lin et al., "Achromatic metalens array for full-colour light-field imaging," *Nat. Nanotechnol.* **14**, 227–231 (2019).
34. H. Kwon et al., "Single-shot quantitative phase gradient microscopy using a system of multifunctional metasurfaces," *Nat. Photonics* **14**, 109–114 (2020).
35. N. A. Rubin et al., "Matrix Fourier optics enables a compact full-Stokes polarization camera," *Science* **365**, eaax1839 (2019).
36. B. Xu et al., "Metalens-integrated compact imaging devices for wide-field microscopy," *Adv. Photonics* **2**, 066004 (2020).
37. J. Engelberg et al., "Near-IR wide-field-of-view Huygens metalens for outdoor imaging applications," *Nanophotonics* **9**, 361–370 (2020).
38. T. Li, "New opportunities for metalenses in imaging applications," *Sci. China Phys. Mech. Astron.* **63**, 284231 (2020).
39. Y. Liu et al., "Meta-objective with sub-micrometer resolution for microendoscopes," *Photonics Res.* **9**, 106–115 (2021).
40. Y. Wang et al., "High-efficiency broadband achromatic metalens for near-IR biological imaging window," *Nat. Commun.* **12**, 5560 (2021).
41. E. Tseng et al., "Neural nano-optics for high-quality thin lens imaging," *Nat. Commun.* **12**, 6493 (2021).
42. X. Luo et al., "Recent advances of wide-angle metalenses: principle, design, and applications," *Nanophotonics* **11**, 1–20 (2022).
43. L. Li et al., "Chromatic dispersion manipulation based on metasurface devices in the mid-infrared region," *Chin. Opt. Lett.* **18**, 082401 (2020).
44. J. W. Goodman, *Introduction to Fourier Optics*, Roberts and Company Publishers, Greenwood Village (2005).
45. S. D. Alaruri, "Calculating the modulation transfer function of an optical imaging system incorporating a digital camera from slanted-edge images captured under variable illumination levels: Fourier transforms application using MATLAB," *Optik* **127**, 5820–5824 (2016).
46. L. Nikolova and P. S. Ramanujam, *Polarization Holography*, Cambridge University Press, Cambridge (2009).

Xin Ye is a PhD student working under the supervision of Tao Li at the College of Engineering and Applied Sciences at Nanjing University. She received her BS degree from the University of Shanghai for Science and Technology, Shanghai, China, in 2019. Currently, she is working on metasurface and advanced imaging.

Xiao Qian is a master student working under the supervision of Tao Li at the College of Engineering and Applied Sciences at Nanjing University. He received his BS degree from Anhui University in 2020. Currently, he is working on metasurface devices.

Yuxin Chen is a master student working under the supervision of Tao Li at the College of Engineering and Applied Sciences at Nanjing University. He received his BS degree from Nanjing University in 2019. Currently, he is working on nanofabrications.

Rui Yuan is a PhD student working under the supervision of Wei Hu at the College of Engineering and Applied Sciences at Nanjing University. He received his MS degree in physics from Hebei University of Technology, Tianjin, China, in 2018. His current research interests include liquid crystal-based beam steering, optical phase array, and tunable lens.

Xingjian Xiao is a PhD student working under the supervision of Tao Li at the College of Engineering and Applied Sciences at Nanjing University. He received his BS degree from Nanjing University in 2019. Currently, he is working on advanced imaging and computation.

Chen Chen is an assistant researcher at the College of Engineering and Applied Sciences at Nanjing University. She received her PhD from Nanjing University in 2021. Currently, she is working on metasurface devices.

Wei Hu is currently a professor of optical engineering at Nanjing University. He received his PhD in polymer chemistry from Jilin University, Changchun, China, in 2009. His research interests include liquid crystal materials and optical devices, with a focus on photoalignment-enabled liquid crystalline superstructures, optically addressed spatial light modulators, and liquid crystal telecom/terahertz elements.

Chunyu Huang is an engineer at Collaborative Innovation Center of Advanced Microstructures at Nanjing University. She received her PhD from Jilin University in 2010. Currently, she is working on nanofabrications.

Shining Zhu is a professor at Nanjing University. He received his PhD from Nanjing University in 1996 and is the group leader of Dielectric Superlattice Laboratory. His research interest includes condensed matter optics, quasiphase matching physics and nonlinear optics, optoelectronic functional materials, quantum optics, and metamaterials.

Tao Li is a professor at the College of Engineering and Applied Sciences at Nanjing University. He received his PhD from Nanjing University in 2005. His research interest includes metamaterials, plasmonics, and nanophotonic integrations.